



# Controlling interfacial protein adsorption, desorption and aggregation in biomolecular condensates

Received: 31 January 2025

Accepted: 2 October 2025

Published online: 19 November 2025

Brent S. Visser <sup>1,5</sup>, Merlijn H. I. van Haren <sup>1,5</sup>, Wojciech P. Lipiński <sup>1,2,5</sup>,  
Kirsten A. van Leijenhorst-Groener<sup>3</sup>, Mireille M.A.E. Claessens <sup>3</sup>,  
Marcos V. A. Queirós <sup>1,4</sup>, Carlos H. I. Ramos <sup>4</sup>, Jorine Eeftens <sup>2</sup> &  
Evan Spruijt <sup>1</sup>

Check for updates

Aggregation of amyloidogenic proteins is linked to age-related diseases. The presence of interfaces can affect their aggregation mechanism, often speeding up aggregation.  $\alpha$ -Synuclein ( $\alpha$ Syn) can adsorb to biomolecular condensates, leading to heterogeneous nucleation and faster aggregation. Understanding the mechanism underlying localization of amyloidogenic proteins at condensate interfaces is crucial for developing strategies to prevent or reverse their binding. We show that  $\alpha$ Syn localization to the surface of peptide-based heterotypic condensates is an adsorption process governed by the protein's condensate-amphiphilic nature, and the condensate surface charge. Adsorption occurs reversibly in multiple layers and plateaus at micromolar concentrations. Based on these findings, we rationally design three strategies to modulate  $\alpha$ Syn accumulation: (i) addition of biomolecules that decrease the condensate  $\zeta$ -potential, such as NTPs and RNA, (ii) competitive adsorption of proteins targeting the condensate interface, such as G3BP1, DDX4-YFP, EGFP-NPM1, Hsp70, Hsc70, and (iii) preferential adsorption of  $\alpha$ Syn to membranes. Removing  $\alpha$ Syn from the condensate interface slows aggregation, highlighting potential cellular control over protein adsorption and implications for therapeutic strategies.

Cells constantly monitor the state of their proteome to ensure that misfolded or aggregated proteins are refolded or cleared. The accumulation of aggregated proteins can lead to severe cellular dysfunction, and ultimately result in diseases such as Alzheimer's and Parkinson's disease<sup>1–5</sup>. Interfaces can influence protein aggregation by serving as catalysts for heterogeneous nucleation. The influence and importance of interfaces on aggregation of proteins related to neurodegenerative diseases has been studied in the past<sup>6</sup>, using solid surfaces<sup>7</sup>, lipid membranes<sup>8</sup>, and water-air interfaces<sup>9,10</sup>. More recently,

biomolecular condensate interfaces were found to also accumulate these proteins, and nucleate protein aggregation at their interface<sup>11–13</sup>. Linsenmeier et al. showed that formation of hnRNPA1 fibrils on idemetic condensates consisting of hnRNPA1 takes place at the condensate interface, and that this process could be reduced by introducing protein-based surfactants<sup>13</sup>. Shen et al. observed that liquid-to-solid transition of FUS condensates is also initiated at their interface<sup>12</sup>. He et al. showed that FUS aggregates grow on the condensate's surface<sup>14</sup>. However, the mechanism underlying interfacial localization remains

<sup>1</sup>Institute for Molecules and Materials, Radboud University, Nijmegen, The Netherlands. <sup>2</sup>Radboud Institute for Molecular Life Sciences, Radboud University, Nijmegen, The Netherlands. <sup>3</sup>Nanobiophysics, Faculty of Science and Technology, MESA+ Institute for Nanotechnology and Technical Medical Centre, University of Twente, Enschede, The Netherlands. <sup>4</sup>Instituto de Química, Universidade Estadual de Campinas (UNICAMP), Campinas, São Paulo, Brazil.

<sup>5</sup>These authors contributed equally: Brent S. Visser, Merlijn H. I. van Haren, Wojciech P. Lipiński. e-mail: [evan.spruijt@ru.nl](mailto:evan.spruijt@ru.nl)

poorly understood, and general strategies to prevent or reverse interfacial protein localization are lacking.

Biomolecular condensates have a non-zero surface charge, either because they are composed of charged biomolecules<sup>15</sup>, or because of asymmetric binding of ions<sup>16,17</sup>. This has been shown using *in vitro* systems, where the ratio of components in biologically relevant condensates determines surface charge<sup>15,18,19</sup>. In biological condensates, it is plausible that condensates also exhibit surface charge, due to different ratios of RNA:protein in different phases of condensates<sup>20</sup>, dynamic compositions over time<sup>21</sup>, and heterogeneity between individual condensates<sup>22,23</sup>. Many disordered, aggregation-prone proteins have charged patches, such as  $\alpha$ -synuclein ( $\alpha$ Syn)<sup>11</sup>, tau<sup>24</sup>, FUS<sup>25</sup>, prion protein<sup>26</sup>, and TDP-43<sup>27</sup>, which could lead to attraction to the charged interface of the condensates.  $\alpha$ Syn specifically is known to localize to charged membrane surfaces<sup>28</sup>, a property that can either enhance or inhibit its aggregation depending on the lipid-to-protein ratio<sup>29</sup>. We hypothesize that surface charge of condensates can govern the interfacial localization of (disordered) proteins, and thus holds a key to preventing or reversing localization and heterogeneous nucleation-based aggregation.

Here, we study how model condensates with tunable  $\zeta$ -potential accumulate wild-type  $\alpha$ Syn at their interface, and how it can be controlled. Our pLys/pGlu *in vitro* condensate model system allows us to finely control parameters and use techniques that are not available to *in vivo* systems, such as single-droplet  $\zeta$ -potentials, optical-trap fusion times, active rheology viscosities, and Raster Image Correlation Spectroscopy. We specifically investigate how the condensate  $\zeta$ -potential governs interfacial protein localization, including  $\alpha$ Syn and TDP-43, by measuring the charge of the interface prior to and after addition of the proteins. We demonstrate for the first time that protein adsorption follows a Freundlich-type adsorption isotherm, suggesting that the condensate interface exhibits heterogeneous binding sites arranged in multiple layers with a finite overall binding capacity. We use this knowledge to rationally design strategies to reverse protein adsorption at the condensate interface.

We present three biologically relevant strategies to control  $\alpha$ Syn interfacial localization, and, thereby, aggregation: (i) addition of biomolecules that can alter the  $\zeta$ -potential of condensates, such as NTPs or RNA, (ii) competitive adsorption of proteins targeting the condensate interface, such as G3BP1, DDX4-YFP, EGFP-NPM1, Hsp70, and Hsc70, (iii) preferential adsorption of  $\alpha$ Syn to membranes, sequestering them away from the condensate interface. These findings indicate that condensate  $\zeta$ -potential and electrostatic interactions can govern accumulation of proteins at condensate interfaces and pave the way for strategies to control protein localization to condensate interfaces and prevent protein aggregation.

## Results

### $\alpha$ Syn localization is governed by $\zeta$ -potential and protein amphiphilicity

We use model condensates with tunable  $\zeta$ -potential, consisting of poly-D,L-lysine with 100 residues and poly-D,L-glutamate with 100 residues (further termed pLys/pGlu) to investigate the role of  $\zeta$ -potential in the localization of amyloidogenic proteins at condensate interfaces. We recently showed that wild-type  $\alpha$ Syn can be accumulated at the interface of pLys/pGlu condensates, leading to substantially enhanced rates of  $\alpha$ Syn aggregation, specifically showing higher elongation and secondary nucleation<sup>11</sup>.  $\alpha$ Syn is a protein consisting of an active aggregation core, flanked by a positively charged disordered N-terminal fragment and a negatively charged disordered C-terminal tail (Fig. 1a)<sup>11</sup>. To gain more insight into  $\alpha$ Syn interfacial localization, we first measured the localization of various  $\alpha$ Syn mutants. Removal of the C-terminal domain drastically changes  $\alpha$ Syn localization: the wild-type protein (computed  $pI = 4.67$ ; charge at pH 7.4 is  $-9.7$ ) accumulates at the surface of

pLys/pGlu droplets, while a variant without the negatively charged C-terminal domain,  $\alpha$ Syn(1–108) (computed  $pI = 9.16$ ; charge at pH 7.4 is  $+2.29$ )<sup>30,31</sup>, was excluded from both the surface and the droplet interior (Fig. 1b)<sup>11</sup>. We also studied the partitioning of  $\alpha$ Syn(60–140), which lacks the disordered, positively charged N-terminal domain (computed  $pI = 4.05$ ; charge at pH 7.4 is  $-12.44$ ).  $\alpha$ Syn(60–140) partitioned into droplets but did not accumulate at the interface (Fig. 1b).  $\alpha$ Syn is thus amphiphilic to condensates, containing charged patches that prefer the interior of the condensate (residues 1–59) and parts that prefer the dilute phase (residues 109–140), causing its interfacial accumulation<sup>11</sup>.

We then assessed how the accumulation of  $\alpha$ Syn at the surface of condensates affects their  $\zeta$ -potential by microelectrophoresis<sup>15</sup>. pLys/pGlu condensates had a  $\zeta$ -potential of  $+8.1 \pm 0.9$  mV, which decreased to zero upon addition of  $\alpha$ Syn in a sigmoidal manner, characteristic of an adsorption isotherm (Fig. 1c). To investigate the mode of interfacial adsorption, we measured the partitioning of  $\alpha$ Syn at different concentrations, keeping the concentration of Alexa Fluor 647-labeled S9C  $\alpha$ Syn (Alexa-647- $\alpha$ Syn) constant when the total concentration was above 3  $\mu$ M (Supplementary Fig. 2). From this, a partition coefficient ( $K_p$ ) was calculated, which shows that the relative concentration of  $\alpha$ Syn at the interface decreases as the total concentration increases (Fig. 1d, e).

With increasing total concentration of  $\alpha$ Syn, the amount of  $\alpha$ Syn at the interface starts to level off, as can be seen upon plotting the calculated interfacial concentration against total concentration of  $\alpha$ Syn. We found that the amount of  $\alpha$ Syn at the condensate interface is described best with the adapted Freundlich isotherm (Fig. 1f). Alternative commonly used adsorption isotherms, such as Langmuir or BET models, performed worse as judged by the Bayesian information criterion (Supplementary Figs. 3 and 4). This suggests that the binding sites at the condensate interface are heterogeneous and multilayered. This is not the case for all condensate systems and interfacial proteins, as very recently Leurs et al.<sup>32</sup> showed a monolayer of GFP-Tau on similar condensates. We interpret this as a reflection of the presence of a transition region in between the condensate interior and the surrounding solution. Based on the magnitude of the condensate interfacial tension, the width of the condensate interfacial region of condensates is estimated to be large, compared to the size of a single protein.

The density and conformation of the condensate components change gradually across this interfacial region<sup>33,34</sup>. Proteins such as  $\alpha$ Syn can adsorb both close to the surrounding dilute phase, where the interaction density is low, and deeper into the interfacial region, closer to the condensate bulk, where the interaction density is higher and the number of unbound sites that are available for binding may be lower. Based on literature, condensate interfaces are typically between 5 and 15 nm in width based on various types of simulated condensates, allowing for multiple  $\alpha$ Syn molecules to fit in this region<sup>33,35–37</sup>. Taking the interfacial heterogeneity into account, the condensate interface has a finite overall capacity for adsorption, and the Freundlich isotherm allows us to compare the binding capacity of the condensates (reflected by the parameter  $S_{sat}$ ), as well as the characteristic interaction strength between the studied systems (reflected by  $n$  see also Supplementary Information, Explanation of fitting of adapted Freundlich model).

Neutralization of the positive  $\zeta$ -potential by negatively charged  $\alpha$ Syn suggests that the adsorption is driven by electrostatic attraction. To test this hypothesis, we altered the condensate  $\zeta$ -potential by changing the mixing ratio of pLys and pGlu. The  $\zeta$ -potential of pLys/pGlu condensates at a 1:2 mixing ratio is negative ( $-1.3 \pm 0.3$  mV), while at a 1.6:1 mixing ratio it is highly positive ( $+8.1 \pm 0.5$  mV, Fig. 2a). Theoretical work by Majee et al. showed that at equal molar ratios, charged condensate interfaces can occur due to unequal gradients of charged molecules at the interface, leading to a net charge, explaining

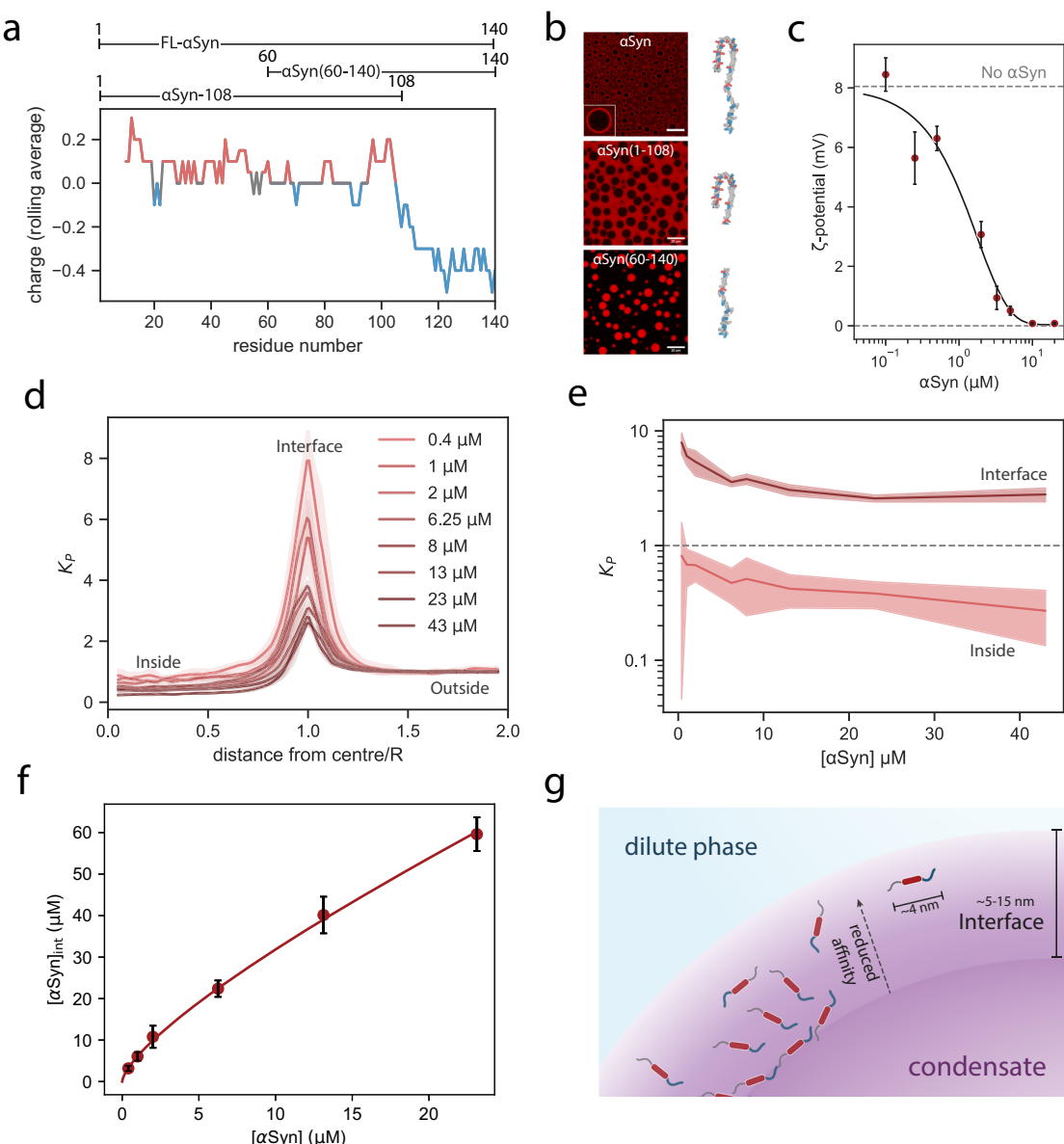


**Fig. 1 |** αSyn adsorbs to positively charged pLys/pGlu condensates and neutralizes the condensate ζ-potential. **a** Moving average of the charge distribution of αSyn and three variants used in this paper, αSyn, αSyn(60–140), and αSyn-108. 3D model of full-length αSyn bound to a micelle (PDB ID 1XQ8), negatively charged amino acids are shown in blue and positively charged amino acids in red<sup>26</sup>. The S9C variant was used for labeling. **b** αSyn is condensate-amphiphilic and depending on which domains of the protein are present can localize to the interface (WT), dilute (1–108), or condensed phase (60–140). Scale bars are 20 μm. **c** Addition of αSyn to pLys/pGlu condensates reduces the condensate ζ-potential in a concentration-dependent manner. (n (left-to-right) = 55, 78, 45, 124, 227, 41, 90, 90 individual droplets from left to right, data shown as mean +/- SD). A sigmoidal fit of the data is shown. **d** Average αSyn partitioning ( $K_p$ ) profile of the condensate. Average of radial

intensity profile of 6 droplets. The interfacial regime has a thickness corresponding to a diffraction limited resolution. Units on the x-axis are distance normalized by the condensate size. (n = 6 droplets, data shown are mean and shaded regions indicate the SD). **e** Partitioning of αSyn and interfacial binding for different concentrations of αSyn. Partitioning to both interface and inside is reduced upon addition of more αSyn. (n = 6, data shown are mean and shaded regions indicate the SD). **f** Microscopically measured interfacial concentration of αSyn with Freundlich isotherm fitted to the datapoints ( $S_{sat} = 84 \pm 37 \mu\text{M}$ ,  $n = 1.58 \pm 0.14$ ). (n = 6 droplets, data shown as mean +/- SD). **g** Schematic drawing of the interfacial region of the condensates with multiple binding sites for αSyn with different affinities. Protein size shown is the radius of gyration of αSyn<sup>27</sup>.

the positive ζ-potential of pLys/pGlu condensates at 1:1 ratio<sup>17</sup>. We found that αSyn remained in the dilute phase for ratios lower than 1:1.4 pLys/pGlu (Fig. 2b and Supplementary Fig. 5). The relative amount of αSyn at the condensate interface and its interior, reflected by  $K_p$ , increased with increasing ζ-potential and reached a plateau at the mixing ratio where the ζ-potential also reached a plateau (Fig. 2c). Fitting Freundlich isotherms to the data at different pLys/pGlu ratios shows that changing the ratio of condensate components alters the affinity of the surface to αSyn (Fig. 2d). Both the interaction strength

and binding capacity increase drastically with increasing pLys (Supplementary Fig. 6).

If αSyn localization is driven by electrostatic interactions, charge screening would weaken the attraction and reduce αSyn accumulation at the interface. Indeed, increasing NaCl only slightly reduced ζ-potential, but it drastically reduced αSyn adsorption at the interface (Fig. 2e, f). Above 250 mM NaCl, αSyn did not adsorb at all, while the  $K_p$  of αSyn inside the condensates decreased to approximately 0.15 (Fig. 2g). Freundlich fits show that increasing NaCl concentration also

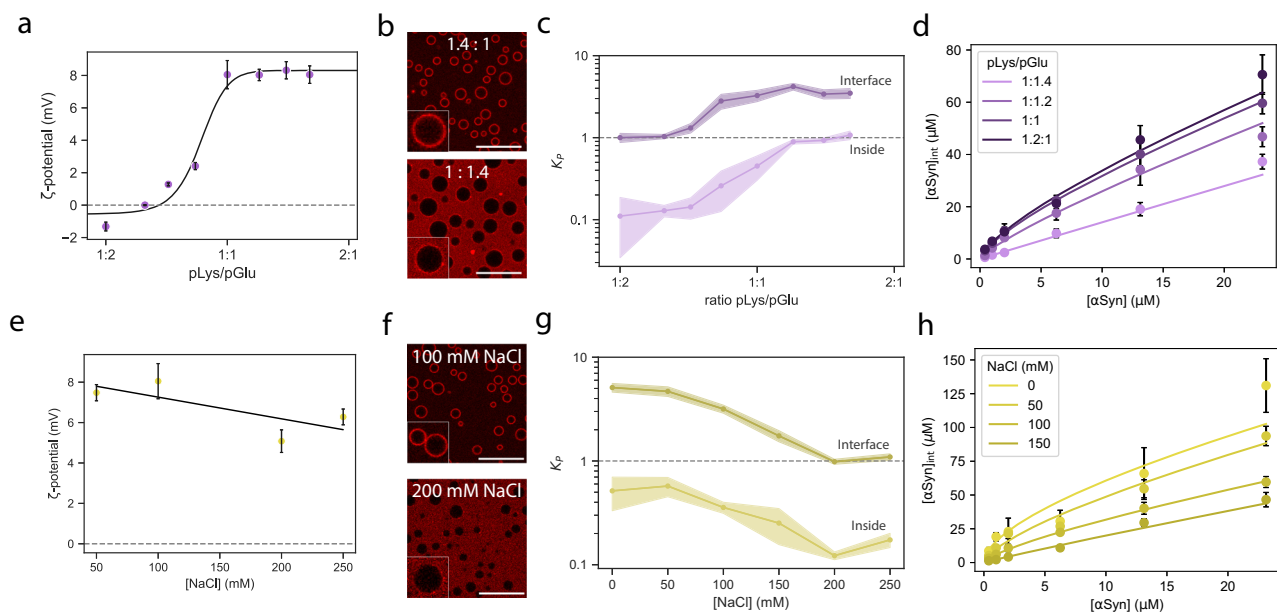


**Fig. 2 | Changing the condensate  $\zeta$ -potential and screening electrostatic interactions reduces the localization of  $\alpha$ Syn on the coacervate interfaces.**

a The  $\zeta$ -potential of pLys/pGlu condensates is dependent on the mixing ratio of polymers. Increasing the amount of pGlu or pLys decreases or increases the charge, respectively. Condensates are positively charged at a neutral mixing ratio (1:1). ( $n$  (left-to-right) = 168, 213, 331, 55, 156, 112, 105, 34 individual droplets, data shown as mean  $\pm$  SD). b Confocal microscopy shows that  $\alpha$ Syn accumulates at the interface of positively charged condensates but not at the interface of negatively charged ones. (Scale bar = 20  $\mu$ m). c Partition coefficient ( $K_p$ ) of  $\alpha$ Syn to the inside and surface of condensates. Data shown as mean with shaded regions indicating SD. d Microscopically measured interfacial concentration of  $\alpha$ Syn with Freundlich

isotherm fitted to the datapoints for 4 ratios of pLys/pGlu ( $n$  = 6 droplets, data shown as mean  $\pm$  SD). e The  $\zeta$ -potential of pLys/pGlu droplets slightly decreases with an increase in NaCl concentration. A linear fit of the data is shown. ( $n$  (left-to-right) = 50, 80, 55, 191, 47 individual droplets, data shown as mean  $\pm$  SD).

f Microscopy shows that an increase of NaCl decreases the interfacial accumulation of  $\alpha$ Syn on the condensate interface. (Scale bar = 20  $\mu$ m). g Partitioning of  $\alpha$ Syn at the interface and to the interior of pLys/pGlu decreases with addition of NaCl. ( $n$  = 6 droplets, data shown are mean and shaded regions indicate the SD).

h Microscopically measured interfacial concentration of  $\alpha$ Syn with Freundlich isotherm fitted to the datapoints for 4 concentrations of NaCl. ( $n$  = 6 droplets, data shown as mean  $\pm$  SD).

reduces both the binding capacity (Fig. 2h,  $S_{\text{sat}} = 333 \mu\text{M}$  to  $S_{\text{sat}} = 9.69 \mu\text{M}$ ) and interaction strength ( $n = 1.86$  to  $n = 1.15$ , Supplementary Fig. 6). We confirmed that this NaCl concentration could effectively screen the electrostatic interactions between  $\alpha$ Syn and pLys by measuring the diffusion of fluorescently labelled  $\alpha$ Syn bound to pLys with increasing NaCl concentration using Raster Image Correlation Spectroscopy (Supplementary Fig. 7)<sup>38</sup>. At 200 mM NaCl,  $\alpha$ Syn diffusion in the presence of pLys was comparable to its diffusion without pLys, indicating that  $\alpha$ Syn is no longer bound to pLys.

We hypothesized that similar driving forces can also cause interfacial localization of other condensate-amphiphilic proteins with charged patches. We therefore also examined the partitioning of TDP-43-TEV-mCherry, which is known to exhibit disordered domains with a net negative and positive charge<sup>39</sup>, in combination with pLys/pGlu condensates. Similar to  $\alpha$ Syn, TDP-43-TEV-mCherry preferentially partitioned to the interface of the droplets (Supplementary Fig. 8).

### NTPs and oligonucleotides can regulate condensate $\zeta$ -potential and remove $\alpha$ Syn

Our results indicate that condensate interfaces exhibit heterogeneous, multilayered adsorption sites and that adsorption to these interfaces is an equilibrium process driven by charge complexation that can be reversed. Therefore, we set out to design strategies to regulate the adsorption and investigate the possibility of selective removal of  $\alpha$ Syn from the interface. In a biological context, cells could (i) modulate condensate  $\zeta$ -potential by regulating the levels of NTPs and metabolites, (ii) express proteins that compete for adsorption to condensate interfaces or form a new condensed phase at the interface, or (iii) exploit the sequestration of proteins by other cellular interfaces, such as membranes. We chose NTPs, metabolites, proteins, and liposomes

as model components because they are charged molecules that are abundant in cells and represent mechanisms by which cells could modulate interfacial charge to control protein localization and aggregation.

We first tested the effect of NTPs, which are present at relatively high concentrations within cells, with ATP being the most abundant at concentrations of ~2 mM, surpassing the Michaelis constant of enzymes by two orders of magnitude<sup>40-45</sup>. We added ATP to pLys/pGlu condensates at physiologically plausible concentrations, and found that above 0.5 mM ATP,  $\alpha$ Syn was excluded from the condensate interface, resulting in a threefold decrease in  $K_p$  at the interface (Fig. 3a, b). Addition of ATP also caused a decrease in  $\alpha$ Syn partitioning inside the condensate, with a  $K_p$  of 0.5 in the absence of ATP and 0.1 at ATP concentrations of 1 mM and higher (Fig. 3b). The condensate  $\zeta$ -potential also decreased from  $+8.1 \pm 0.9$  mV at 0 mM ATP to  $-3.0 \pm 0.8$  mV at 5 mM (Fig. 3c). This lower and negative  $\zeta$ -potential weakens the electrostatic interactions of  $\alpha$ Syn with the condensate surface, causing  $\alpha$ Syn to be released into the surrounding dilute phase. Furthermore,  $\alpha$ Syn localization is reversible, as most of the  $\alpha$ Syn releases from the interface after adding ATP (Supplementary Fig. 9). We also observed that partitioning of  $\alpha$ Syn(60–140) was not substantially affected by the addition of ATP, confirming that ATP mainly affects interfacial accumulation (Supplementary Fig. 1). Addition of ATP had no substantial effect on interfacial tension and viscosity (Supplementary Figs. 10 and 11). Interfacial  $\alpha$ Syn with increasing ATP can also be described by the Freundlich isotherm, reaching a  $S_{\text{sat}}$  value of ~20  $\mu\text{M}$  and  $n$  of 1.1 (Fig. 3d and Supplementary Fig. 6).

Besides ATP, we added other NTPs to see if they have a similar effect on the  $\zeta$ -potential of pLys/pGlu condensates. Addition of 5 mM GTP led to droplets with a  $\zeta$ -potential of  $-3.5 \pm 0.2$  mV, similar to ATP

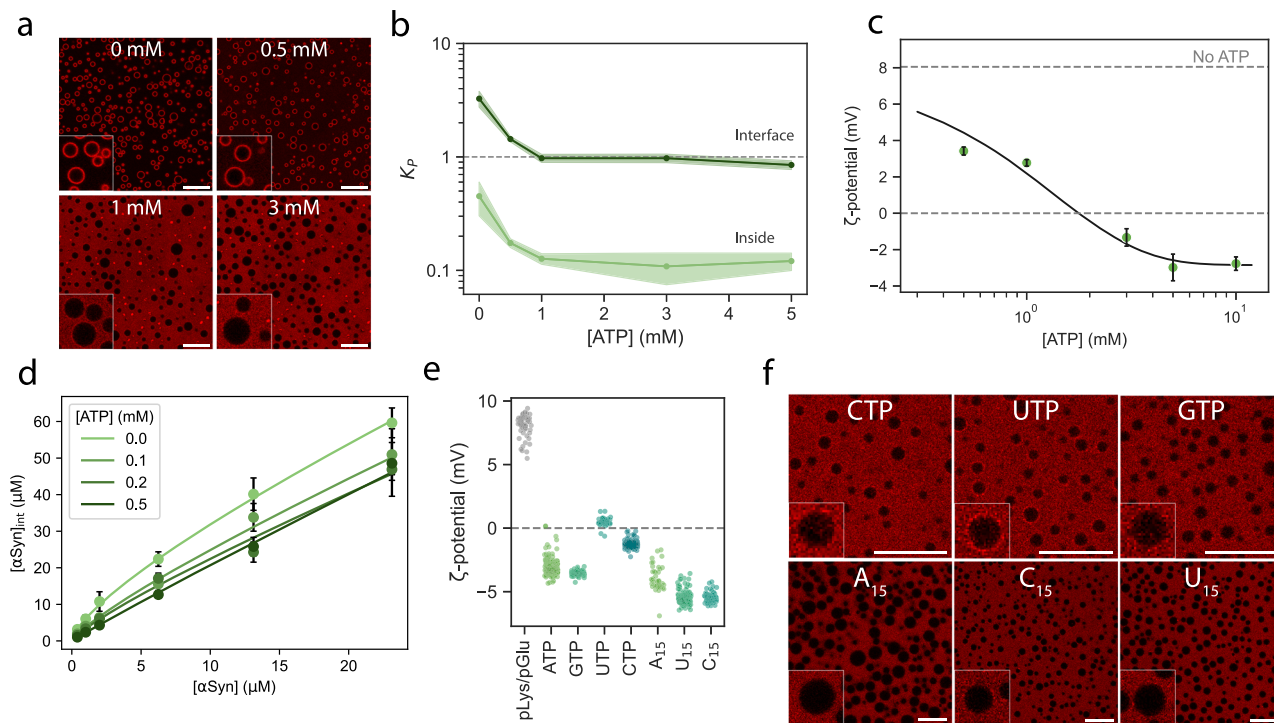


**Fig. 3 | NTPs and RNA change the  $\zeta$ -potential of pLys/pGlu condensates and decrease interfacial  $\alpha$ Syn accumulation.** **a**  $\alpha$ Syn is delocalized from the pLys/pGlu condensate interface by addition of ATP. (Scale bar = 20  $\mu$ m). **b** The partition coefficient  $K_P$  of  $\alpha$ Syn is reduced by the addition of ATP, both at the interface and inside of the condensates. ( $n = 6$  droplets, data shown are the mean and shaded regions indicate the SD). **c** ATP causes a decrease in the  $\zeta$ -potential of pLys/pGlu droplets ( $n$  (left-to-right) = 55, 154, 114, 44, 142, 95 individual droplets, data shown

as mean  $\pm$  SD). A sigmoidal fit of the data is shown. **d** Freundlich model fits of  $\alpha$ Syn adsorption for different ATP concentrations. A decrease in the binding capacity of the surface can be seen as more ATP is added. ( $n = 6$  droplets, data shown as mean  $\pm$  SD). **e** Addition of NTPs (5 mM) and RNAs (0.1 mM) reduces the  $\zeta$ -potential of pLys/pGlu condensates ( $n$  (left-to-right) = 55, 142, 62, 38, 186, 42, 110, 55 individual droplets). **f** NTPs (5 mM) and RNA oligos (0.1 mM) lead to removal of most of  $\alpha$ Syn from the interface. (Single experiment results, scale bar = 20  $\mu$ m).

(Fig. 3e). The pyrimidines CTP and UTP had a weaker effect than the purines, but still lowered the  $\zeta$ -potential. All NTPs prevented  $\alpha$ Syn interfacial accumulation to a large extent (Fig. 3f). Next, we set out to study the influence of short RNA oligonucleotides on the condensate  $\zeta$ -potential, as their multivalency could enhance the charge reversal observed with NTPs. We selected A<sub>15</sub>, C<sub>15</sub>, and U<sub>15</sub> and added them to pLys/pGlu condensates. As expected, oligonucleotides could also invert the  $\zeta$ -potential of condensates at a concentration of 0.1 mM, and they were able to displace  $\alpha$ Syn from the droplet interface (Fig. 3e, f).

We also compared the interfacial accumulation of TDP-43-TEV-mCherry on pLys/pGlu condensates with and without 5 mM ATP. Supporting our previous findings, ATP also decreased the accumulation of TDP-43-TEV-mCherry, although it did not completely remove the protein (Supplementary Fig. 8), possibly because TDP-43 was already partially aggregated.

The effect of low concentrations of NTPs and oligonucleotides on protein adsorption to condensates shows the potential to control protein localization based on electrostatic interactions, which could prevent heterogeneous nucleation at the condensate interface. These results suggest that electrostatic interactions may be a common factor in determining protein localization and that cells may use strategies like ATP production to manipulate condensate interface properties and protein localization.

#### Proteins can displace $\alpha$ Syn by competitive adsorption

We then investigated if competitive adsorption at the condensate interface is possible, and if other proteins could displace  $\alpha$ Syn from the interface. We investigated the condensate surface targeting potential of a number of commonly studied, partially disordered proteins with negatively charged patches (Supplementary Fig. 12).

namely GFP-G3BP1, DDX4-YFP, EGFP-NPM1, and TDP-43-TEV-mCherry, and two heat shock proteins, Hsc70 and Hsp70, which are known to interact with  $\alpha$ Syn<sup>46–50</sup>.

Most of these proteins were found to localize at the interface of pLys/pGlu condensates (Fig. 4a). Strikingly, they were able to reduce the concentration of  $\alpha$ Syn at the interface. The degree of displacement of  $\alpha$ Syn (as measured by reduction in the  $K_P$  to the interface) varied between proteins (Fig. 4b) and many co-localized with  $\alpha$ Syn (Supplementary Fig. 13a), suggesting that their binding strength to the interface was comparable to  $\alpha$ Syn. The molecular chaperones, Hsc70 and Hsp70, also co-localize with  $\alpha$ Syn at the interface, potentially allowing for enhanced chaperone functionality<sup>51–53</sup> and reducing the aggregation propensity of  $\alpha$ Syn, without necessarily displacing it completely from the condensate interface. We also observe that the chaperones localize to the interface more strongly when  $\alpha$ Syn is present, showing potentially targeted accumulation (Supplementary Fig. 14). These findings show that proteins at the condensate interface are in competition with each other for binding sites.

Surprisingly, the addition of DDX4-YFP, GFP-G3BP1, and EGFP-NPM1 led to the formation of multiphase condensates when added to the pLys/pGlu condensates, resulting in  $\alpha$ Syn partitioning in the newly formed outer phase with high colocalization. A reason for this additional phase separation is the amphiphilic nature of these proteins, as they contain a phase-separating domain and a solubilizing domain in the form of the fluorescent tag<sup>54</sup>. For EGFP-NPM1, we observe multiphase condensate formation at 12.5  $\mu$ M (Fig. 4c and Supplementary Fig. 15a), and high partitioning of  $\alpha$ Syn into the new phase (Fig. 4d,  $K_P = 12$ ). The colocalization of NPM1 and  $\alpha$ Syn increases with NPM1 concentration (Supplementary Figs. 13b and 15). Multiphase condensates can potentially function as a compartment capable of

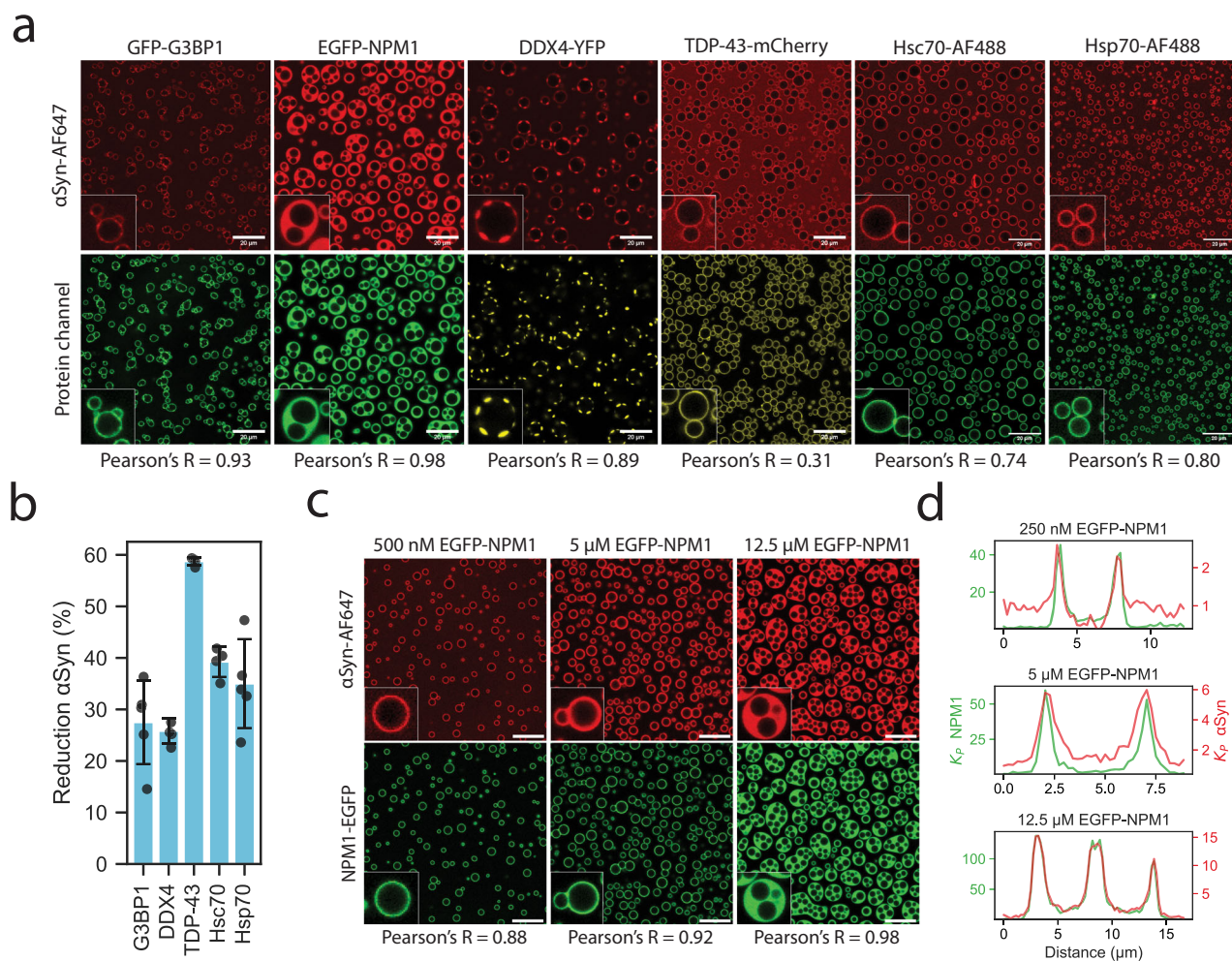


**Fig. 4 | Localization of various proteins to the interface of pLys/pGlu condensates with αSyn.** **a**, GFP-G3BP1, EGFP-NPM1, DDX4-YFP, and TDP-43-TEV-mCherry localize to the interface of the condensates competing with the interfacial αSyn. Notably, NPM1 and DDX4 form a distinct third phase around the condensates, which also sequesters αSyn. Pearson's correlation coefficients are shown to quantify colocalization. (Scale bar = 20 μm). **b**, Percentage reduction of the αSyn intensity at the interface in the presence of selected competing interfacial proteins.

All proteins reduced αSyn intensity at the interface ( $n=5$  droplets for αSyn and Hsp70,  $n=4$  for other conditions; data shown as mean  $\pm$  SD). **c**, EGFP-NPM1 forms multiphase condensates at 12.5 μM, which sequester αSyn. (Scale bar = 20 μm). **d**, Line profiles of EGFP-NPM1 (green) and αSyn (red). The partition coefficient ( $K_p$ ) of both EGFP-NPM1 and αSyn increases with higher concentrations, and both colocalize in the multiphase condensates.

sequestering αSyn to remove it from the condensate interface<sup>11</sup>. We found that the ζ-potential decreased with increasing EGFP-NPM1 and became negative around 2.5 μM, even before the separate new phase is visible by microscopy (Supplementary Fig. 16). This is remarkable, as αSyn was not able to invert the droplet ζ-potential. We hypothesize that EGFP-NPM1 already forms a new microphase that is spread at the interface of the pLys/pGlu condensates and that sequesters αSyn. This newly formed liquid phase has a negative ζ-potential, providing a separate mechanism of removing αSyn from the pLys/pGlu condensate interface.

#### Membranes can sequester αSyn away from condensate interfaces

Lastly, we investigated αSyn localization in the presence of a second interface to which the protein could adsorb. One effect of membrane surfaces may be to prevent interfacial localization of αSyn to charged condensates, due to preferential adsorption to the membranes, as the canonical role of αSyn is thought to involve membrane binding<sup>28,55</sup>. Membrane-bound αSyn displays distinct conformations from monomeric αSyn<sup>56</sup>, sometimes leading to delayed aggregation and

nonparticipation in aggregation<sup>57</sup>. In vitro, it has been shown that αSyn can also bind cooperatively to unilamellar liposomes<sup>58,59</sup>. We prepared vesicles with two lipid compositions, DOPG/DOPC 1:1 and DOPG/DOPC/DOPE 1:2:1 (Supplementary Fig. 17) and added them to the condensates with αSyn.

Using labeled liposomes, we observed that liposomes of both compositions partition to the interface at low concentrations, and into the condensates at higher concentrations (Fig. 5a). We found that the liposomes lowered the ζ-potential of the condensates, but that they remained net positively charged (Fig. 5b). However, αSyn no longer localized to the condensate interface when the liposomes partition into the condensates. In contrast to other experiments with such positive condensates, αSyn partitions into the condensates and colocalizes with the liposomes (Fig. 5c). We hypothesize that αSyn is sequestered by the membrane surface and is pulled into the condensates by the vesicles. It remains to be investigated whether the vesicles remain intact upon partitioning into the condensates. No substantial differences between the two compositions of liposomes were observed in the partitioning, despite a difference in ζ-potential of the droplets. These results show that competition between interfaces

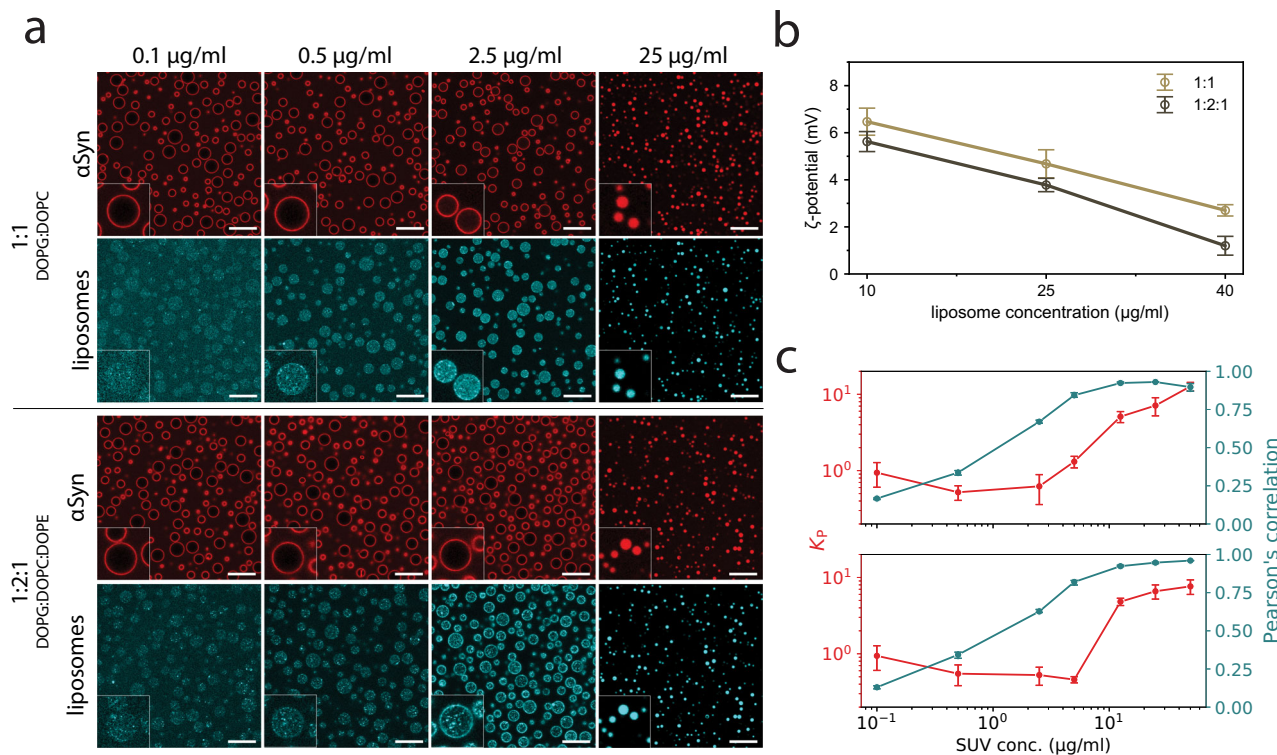


**Fig. 5 | Liposomes partition into pLys/pGlu condensates and drive partitioning of  $\alpha$ Syn.** **a** Liposomes localize to the interface at low concentrations and partition into the condensates at higher concentrations. This leads to co-partitioning of  $\alpha$ Syn above a critical concentration. (Scale bar = 20  $\mu\text{m}$ ). **b**  $\zeta$ -potential of the condensates stays positive after addition of the liposomes. (1:1  $n$  (left-to-right) = 89, 69, 69

individual droplets, 1:2.1  $n$  (left-to-right) = 185, 136, 68 individual droplets data shown as mean  $\pm$  SD). **c** Increasing liposome concentration leads to increased partitioning ( $K_P$ ) of  $\alpha$ Syn (red) and colocalization of  $\alpha$ Syn and the liposomes (blue). ( $n$  = 6 droplets, data shown as mean  $\pm$  SD).

can alter protein localization, which could also serve as a regulatory mechanism in cells, as these interactions are likely protein and condensate specific.

#### Displacement of $\alpha$ Syn from the condensate interface slows down aggregation

We have previously reported that condensate interfaces can act as heterogeneous nucleation sites for  $\alpha$ Syn aggregation<sup>11</sup>. It is also known that air-water interfaces can promote primary nucleation events<sup>60</sup> and that positively charged interfaces accelerate aggregation<sup>61</sup>. We therefore expected that removal of  $\alpha$ Syn from pLys/pGlu interface can affect the aggregation kinetics and lead to a reduction in aggregation rates. We used Thioflavin T (ThT) fluorescence assays to follow  $\alpha$ Syn aggregation with condensates in the different scenarios investigated above to remove  $\alpha$ Syn from the condensate interface. Addition of 3 mM ATP substantially slows down  $\alpha$ Syn aggregation in the presence of condensates (Fig. 6a). This effect is observed over a range of  $\alpha$ Syn concentrations, from 5 to 80  $\mu\text{M}$  (Fig. 6b). Increasing the ATP concentration could further slow down  $\alpha$ Syn aggregation up to fivefold (Fig. 6c). While addition of ATP changes the aggregation half-time substantially in the presence of condensates, we find no major influence on the half-time in the absence of condensates, confirming that ATP acts as a modifier of  $\alpha$ Syn-condensate interactions, rather than interacting with  $\alpha$ Syn directly (Supplementary Fig. 18). As a negative control, we examined aggregation of  $\alpha$ Syn(60–140)—which does partition to the interface—and observe that aggregation is not substantially altered due to the addition of ATP (Supplementary Fig. 19). These findings confirm that removal of  $\alpha$ Syn from the interface by addition of ATP can slow down aggregation through removal of the protein from the condensate interface (Fig. 3a and Supplementary Fig. 20).

Since we observed removal of  $\alpha$ Syn not only for ATP but also for other NTPs and small RNA oligos, we investigated whether they could also reduce the aggregation rates. As expected, all of the strategies that removed  $\alpha$ Syn from the interface also slowed down aggregation (Fig. 6d). One of the proteins was also able to slow down aggregation – 20  $\mu\text{M}$  EGFP-NPM1—by forming multiphase condensates that sequester  $\alpha$ Syn (Fig. 6e). In the case of smaller multiphase compartments, we hypothesize that the physicochemical environment did not induce aggregation-slowing conformational changes in  $\alpha$ Syn. We also measured the aggregation kinetics in the presence of liposomes. On average, the addition of liposomes had no substantial effect on the aggregation rate of  $\alpha$ Syn. This can be explained by the fact that  $\alpha$ Syn aggregation can also be enhanced by binding to membranes, similar to its binding to condensate interfaces (Fig. 6f).

We also examined the kinetics of  $\alpha$ Syn aggregation with increased NaCl and altered condensate composition. Interestingly, while NaCl accelerates  $\alpha$ Syn aggregation in solution<sup>62</sup>, it suppresses aggregation of  $\alpha$ Syn in the presence of condensates (Supplementary Fig. 21), by removing  $\alpha$ Syn from the interface<sup>62</sup>. Altering the condensate composition also influences  $\alpha$ Syn aggregation rates. As expected, neutral or negatively charged condensates slow down aggregation, whereas positively charged condensates accelerate it.

Finally, we analyzed how nucleation rates and elongation rates change when  $\alpha$ Syn no longer accumulates at the interface of the condensates. We calculated the lag time ( $t_{\text{lag}}$ ) and  $1/V_{\text{max}}$  as kinetic parameters that can serve as proxies for  $k_n$  and  $k_{\text{elong}}$  using methods described previously<sup>11</sup>. We found that the aggregation lag time  $t_{\text{lag}}$  is increased in all situations when  $\alpha$ Syn is removed from the interface, indicating suppression of nucleation (Supplementary Fig. 21). Interestingly, the maximum rate of aggregation is reduced by addition of

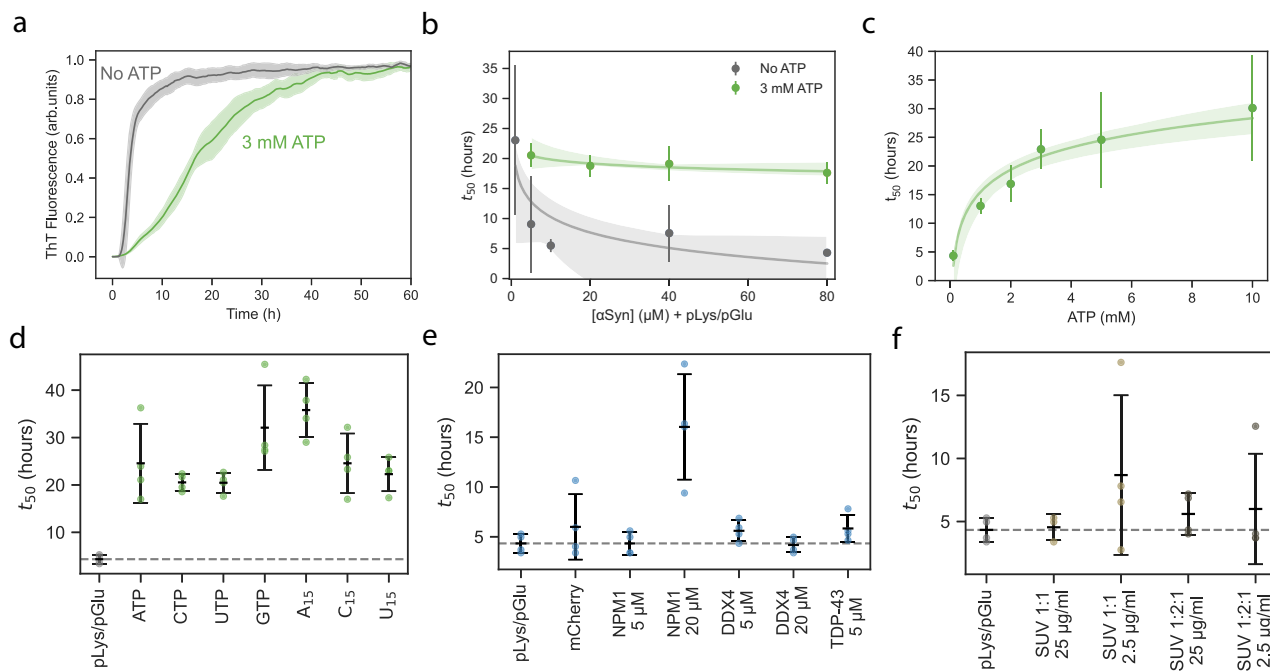


**Fig. 6 | Removal of  $\alpha\text{Syn}$  from the condensate interface with ATP slows down aggregation.** **a** ThT aggregation assays show that the addition of 3 mM ATP to pLys/pGlu condensates substantially slows down aggregation ( $n = 4$  individual wells, data shown as mean with shaded regions representing SD). **b** Increasing the concentration of  $\alpha\text{Syn}$  in the presence of pLys/pGlu condensates speeds up protein aggregation when no ATP is present, but has no effect when 3 mM ATP is present. Exponential decay fits of the data are shown. ( $n = 4$  individual wells, data shown as mean  $\pm$  SD). **c** There is a logarithmic increase in the  $t_{50}$  of aggregation and concentration of ATP. ( $n = 4$  individual wells, data shown as mean  $\pm$  SD). **d** Aggregation of  $\alpha\text{Syn}$  with pLys/pGlu condensates is slowed down by the presence

NTPs (5 mM) or RNA oligos (0.125 mM) compared to the reference sample. ( $n = 4$ , black line indicates mean  $\pm$  SD). **e** Proteins that co-localize to the interface of pLys/pGlu condensates with  $\alpha\text{Syn}$  do not substantially alter the aggregation rate. However, the multiphase condensates formed by NPM1 (20  $\mu\text{M}$ ) did slow down aggregation. ( $n = 4$  individual wells, black line indicates mean  $\pm$  SD). **f**  $\alpha\text{Syn}$  aggregation with pLys/pGlu condensates in the presence of DOPG/DOPC 1:1 and DOPG/DOPC/DOPE 1:2:1 liposomes. The liposomes did not alter aggregation substantially for either concentration. ( $n = 4$  individual wells, black line indicates mean  $\pm$  SD).

NaCl and ATP, but not by altering the pLys/pGlu ratio, potentially due to more pLys being present in the dilute phase.

These analyses imply that  $\alpha\text{Syn}$ , when it is present at the interface, allows for increased nucleation due to a difference in average conformation. To confirm this, we performed dual-label intramolecular FRET. We observed that the FRET efficiency of two variants labeled with Alexa Fluor 488 and 568 (42C–90C and 9C–69C) is highest at the interface compared to the dilute and dense phases. This indicates increased compactness between these positions on the protein at the interface (Supplementary Fig. 22), a finding that is in support of the theoretical predictions from Wang et al.<sup>34</sup>.

## Discussion

Increasing evidence shows the interface of biomolecular condensates influences protein aggregation, including amyloidogenic proteins such as  $\alpha\text{Syn}$ . This applies to aggregating proteins that undergo LLPS within cells on their own, but also to systems in which the aggregating protein is a guest molecule in host liquid condensates formed by other components of the cell. To assess their relevance in pathology and to rationally design strategies to prevent or reverse protein binding to condensate interfaces, we must first understand how the complex intracellular environment affects the properties of liquid interfaces and modulates interactions with aggregating proteins.

In this work, we examined the interactions between a tunable model peptide-based condensate system, pLys/pGlu, and the amyloidogenic protein  $\alpha\text{Syn}$ .  $\alpha\text{Syn}$  binds strongly to the condensate interface when it carries a net positive charge, as observed with microscopy and single droplet  $\zeta$ -potential measurements. We discover that the interface accumulation is an equilibrium adsorption process that follows a

Freundlich isotherm, indicating a multilayered interface with variable binding strengths. This finding has implications for understanding and regulating condensate surface properties, relevant for the fields of biomolecular condensates and in the field of synthetic cells and origins-of-life.

We confirmed that the interfacial charge of pLys/pGlu condensates and the amphiphilic nature of  $\alpha\text{Syn}$  govern the adsorption process. Our findings with the pLys/pGlu model system not only mimic what charged interfaces of cellular condensates could do, but also provide a controlled framework to study how such interfaces may be altered to prevent pathological aggregation.

We then proposed three biochemically relevant strategies to modulate or reverse  $\alpha\text{Syn}$  adsorption to condensate interfaces and studied their effect on the kinetics of  $\alpha\text{Syn}$  aggregation. NTPs and short oligonucleotides decreased the interfacial charge even at low concentrations, and could remove  $\alpha\text{Syn}$  from the condensate interface in a reversible manner. Adding other interfacially adsorbing proteins, such as EGFP-NPM1, DDX4-YFP, and GFP-G3BP1, was found to result in a reduction of  $\alpha\text{Syn}$  at the interface—showing that there is competition for binding sites at the condensate interface—and even the formation of multiphase condensates, providing a more favorable phase for  $\alpha\text{Syn}$  to partition into. Molecular chaperones Hsc70 and Hsp70 co-localize with  $\alpha\text{Syn}$  at the interface of pLys/pGlu condensates, without outcompeting  $\alpha\text{Syn}$  completely from the condensate interface. Finally, liposomes provided an alternative surface for  $\alpha\text{Syn}$  to which it had a higher affinity, resulting in sequestration of  $\alpha\text{Syn}$  away from the interface inside the condensates.

For some of these strategies, we observed substantially reduced  $\alpha\text{Syn}$  aggregation rates. Adding NTPs and oligos slowed down

aggregation up to fivefold, while NTPs did not affect  $\alpha$ Syn in solution. In addition, EGFP-NPM1 multiphase condensates also slowed down  $\alpha$ Syn aggregation. In contrast, the addition of liposomes did not change the rate of  $\alpha$ Syn aggregation, possibly because aggregation can also be enhanced by membrane binding. Our framework and molecular strategies for regulation of protein localization at condensate interfaces not only open the way for better understanding of the interfacial composition of condensates *in vivo*, but also for new approaches to modulate the adverse effects of aggregation-prone proteins at condensate interfaces.

## Method

### Condensate formation

All experiments with poly-D,L-lysine and poly-D,L-glutamate condensates were performed using a HEPES buffer (final concentration 50 mM, pH 7.4) containing 100 mM NaCl and 100  $\mu$ M EDTA unless stated otherwise. Condensates were prepared by adding pLys to the buffer, followed by pGlu, both with a final concentration of 2.4 mM monomer units. Additives such as sodium chloride,  $\alpha$ Syn, and ATP were added directly after, and the samples were mixed by vortexing for 10 s at 2800 rpm (lab dancer, VWR).

### $\alpha$ Syn preparation and labeling

Wild-type  $\alpha$ Syn, and the cysteine mutants were expressed and purified as described elsewhere<sup>33</sup>. Purified proteins were stored at a concentration of ~250  $\mu$ M in 10 mM TRIS-HCl (pH 7.4) at -80 °C, supplemented with 1 mM dithiothreitol (DTT) for the cysteine mutants. Single-labeled proteins were labeled according to the dye manufacturer procedures.

### Protein expression

pHBS834 H14-SUMO-TDP43 WT-TEV-mCherry was a gift from Rajat Rohatgi (Addgene plasmid # 133320; <http://n2t.net/addgene:133320>; RRID: Addgene\_133320)<sup>39</sup>. *Escherichia coli* BL21 (DE3) was transformed with pHBS834 H14-SUMO-TDP43 WT-TEV-mCherry. Overnight cultures were used to inoculate large flasks of LB media, then cells were grown at 37 °C to an OD<sub>600</sub> of 0.5, before protein expression was induced with 50  $\mu$ M IPTG overnight at 15 °C. Prior to harvesting, the pellet was resuspended in lysis buffer (20 mM Tris-HCl pH 8.0, 1000 mM NaCl, 5 mM DTT, 20 mM imidazole) with a cOmplete™, EDTA-free Protease Inhibitor Cocktail.

The resuspended cells were lysed using a homogenizer. The cleared supernatant was loaded onto a 5 ml Cytiva HisTrapFF. The His-tagged protein was eluted using elution buffer (20 mM Tris-HCl pH 8.0, 1000 mM NaCl, 5 mM DTT, 400 mM imidazole). ULP protease was added to cleave the His-SUMO-tag and was dialyzed overnight in a 25 kDa membrane against SEC buffer (40 mM HEPES pH 7.4, 300 mM NaCl, and 1 mM DTT). Finally, the protein was isolated by SEC using a S200 16/600 SEC column. The protein was concentrated to approximately 100  $\mu$ M using 10 kDa spin filters.

Human Hsp70 and Hsc70 were expressed in *E. coli* BL21 (DE3) and Rosetta™ 2(DE3) cells, respectively. The bacteria were left to grow until optical density has reached 0.6–0.8. At this point, 1 mM of IPTG was added, inducing the bacterial culture for 16 h at 16 °C. Cell pellets were obtained by centrifugation and stored at -20 °C. To be lysed, cells were resuspended in appropriate volumes of a buffer containing 20 mM phosphate, 250 mM NaCl, and pH 7.5 (buffer A) + 6 units of DNase and RNase, and 1 capsule of cOmplete™ for 30 min. After that, the suspensions were submitted to ultrasound pulses for a total time of 2 min and followed by centrifugation. Ni-affinity chromatography was performed by loading the lysed solutions onto a 5 ml HisTrap™ columns (Cytiva). The elution of the proteins took place by employing buffer A containing 250 mM imidazole. The fractions containing each chaperone were loaded onto a Superdex™ 200 pg HiLoad™ 16/600

(GE Healthcare), also equilibrated with buffer A. After that, the fractions enriched in the chaperones were analyzed through SDS-PAGE and concentrated by using a centrifugation filter with a 30 kDa molecular weight cutoff.

EGFP-NPM1, a fusion protein of enhanced green fluorescent protein and nucleophosmin-1 was expressed using BL21(DE3) *E. coli* cells transformed with a pET28a(+)EGFP-NPM1 plasmid. Cells were grown at 37 °C to an OD<sub>600</sub> of 0.7 expression was induced with 1 mM IPTG. Cells were lysed using three rounds of sonication (Sanyo Soniprep 150) on ice in cycles of 10 s with an amplitude of 10%. EGFP-NPM1 was purified using a Ni-NTA agarose (Fisher Sci) column, followed by size exclusion chromatography with a HiLoad Superdex 75 26/600 (GE Healthcare)<sup>64</sup>.

DDX4-YFP, a mutated version of the human DDX4 nuage protein, in which its C-terminal helicase domain is replaced by a yellow-fluorescent protein sequence, was expressed using BL21(DE3) *E. coli* cells transformed with a Ddx4NYFP pETM30 plasmid. Cells were lysed using a homogenizer (LTD FPG12800) and clarified cell lysate was purified using a HisTrapFF (Cytiva) column. TEV protease was added to the eluted DDX4-YFP protein and the mixture was dialyzed to SEC buffer (20 mM Tris, 300 mM NaCl, 5 mM TCEP, pH 8.0). The dialyzed product was concentrated and further purified using size-exclusion chromatography with a S200 16/600 SEC column (GE Healthcare)<sup>65</sup>.

### Lipids and liposome preparation

All unlabeled lipids, 1,2-dioleoyl-sn-glycero-3-phosphoglycerol (DOPG) 1,2-dioleoyl-sn-glycero-3-phospho-ethanolamine (DOPE), and 1,2-dioleoyl-sn-glycero-3-phosphocholine (DOPC), were purchased from Avanti Polar Lipids. Atto 488-labeled DOPE was obtained from Sigma Aldrich. Lipid stock solutions were prepared by dissolving in chloroform at 25 mg/ml, evaporating, and re-dissolving in half of the original volume of chloroform for a final concentration of 50 mg/ml for the lipid stock solutions<sup>66</sup>.

DOPG/DOPC 1:1 and DOPG/DOPC/DOPE 1:2:1 liposomes were prepared according to ref. <sup>67</sup>. Lipid solutions were added to chloroform in glass HPLC vials. The mixes were evaporated under argon to dry to a film. Buffer (50 mM HEPES, 100 mM NaCl, 5  $\mu$ M EDTA) was added to each vial. Vials were kept at 40 °C overnight. After incubation, contents were vortexed and extruded 11 times with a 200 nm membrane and 11 times with a 50 nm membrane.

### Preparation of modified glass slides

Samples were imaged in  $\mu$ -Slide 18 Well chambered coverslips (uncoated polymer coverslip, Ibidi). All slides used for microscopy were modified to minimize spreading of the condensates on the surface of the slide. The surface intended to be modified was cleaned with oxygen plasma, and a solution of 0.01 mg/ml PLL-g[3.5]-PEG (SuSoS, Dübendorf, Switzerland) dissolved in 10 mM HEPES buffer (pH 7.4) was applied on the glass immediately after the plasma treatment. Glass was incubated with the PLL-g-PEG solution overnight at room temperature. Subsequently, it was rinsed three times with Milli-Q water and dried with pressurized air. Modified slides were stored at room temperature.

### Confocal microscopy

Localization of labeled proteins was studied using confocal microscopy. A Leica SP8 $\times$  confocal microscope equipped with  $\times$ 100 magnification oil-immersion objective was used. Samples were placed in 18-well chambered glass coverslips (Ibidi GmbH, Germany), previously modified with PLL-g[3.5]-PEG. Partition coefficients were determined by calculating the ratio of fluorescence intensity in the condensed phase to fluorescence intensity in the outer phase (average intensity values from at least 6 droplets and outer phase of a similar area were used). Fluorescence profiles were measured using the ImageJ plugin Radial Profiles Extended and normalized to dilute phase signal. Colocalization was measured using the ImageJ plugin Coloc 2.

## Raster image correlation spectroscopy

The diffusion of  $\alpha$ Syn was determined using Raster Image Correlation Spectroscopy (RICS) on a Leica SP8 confocal microscope equipped with a single-photon detector. Calibration of the focal volume waist  $\omega_0$  was performed using the known diffusion coefficient of Alexa 488 of  $435 \mu\text{m}^2 \text{s}^{-1}$  ( $T = 22.5 \pm 0.5^\circ\text{C}$ ) in water<sup>68</sup>, and  $\omega_z$  was set to 3 times the value of  $\omega_0$ . All measurements were captured at a resolution of  $256 \times 256$  pixels with a  $20 \text{ nm}$  pixel size using a  $63\times$  objective. Analysis of autocorrelation curves was performed in PAM<sup>69</sup>.

## $\zeta$ -potential measurements by microelectrophoresis

All samples were imaged on 6-well  $\mu$ -channel slides (Ibidi) that were modified with  $0.1 \text{ mg/ml}$  PLL-g[3.5]-PEG. Before image acquisition, a  $100 \mu\text{L}$  condensate suspension was transferred to the channel and was incubated for 1 h to allow droplets to coalesce and settle on the glass surface. Electrodes (2 mm, silver) connected with copper wires to a BT-305A PSU direct current power source (Basetech) were lowered into opposing ends of the microchannel slide and an electric field of 1.2 to  $12 \text{ V/cm}$  was applied, with the cathode at the top of the field of view. Moving condensates were imaged in the middle of the channel of the microslide. Samples were imaged on an Olympus IX83 inverted fluorescence microscope equipped with a motorized stage (TANGO, Märzhäuser) and LED light source (pE-4000 CoolLED). Images were recorded with a  $40\times$  universal plan fluorite objective (WD 0.51 mm, NA 0.75, Olympus) with a temperature-controlled CMOS camera (Hamamatsu Orca-Flash 4.0).

Raw microscopy videos were processed and analyzed with MATLAB 2021 Image processing Toolbox and droplet trajectories were determined using methods previously described<sup>15</sup>.  $\zeta$ -potentials for all detected droplets in a sample were determined from their velocities with a modified Smoluchowski equation, using the applied electric field strength, Debye length calculated from salt concentration and the droplet viscosity determined by active rheology. All parameters used to calculate the condensate  $\zeta$ -potential are available in Supplementary Table S1.

## ThT aggregation kinetic assays

To estimate the kinetic parameters of aggregation, we performed standard ThT aggregation assays. Upon binding to  $\beta$ -sheets, ThT fluorescence intensity and the changes in fluorescence are proportional to the mass of aggregate formed<sup>70,71</sup>.

Aggregation assays were performed under the following conditions unless mentioned otherwise:  $50 \text{ mM}$  HEPES (pH 7.4),  $100 \text{ mM}$  NaCl,  $100 \mu\text{M}$  EDTA,  $20 \mu\text{M}$  ThT, and  $40 \mu\text{M}$   $\alpha$ Syn. Protein solutions were filtered using Pierce cellulose acetate filter spin cups (Thermo Fisher Scientific) before every aggregation kinetic assay, and concentration was determined on the basis of absorbance at  $276 \text{ nm}$  ( $\epsilon = 5600 \text{ M}^{-1} \text{ cm}^{-1}$  for wild-type  $\alpha$ Syn). All aggregation assays were performed in non-binding 384-well black-walled plates (Greiner Bio-One GmbH, Austria) at  $37^\circ\text{C}$ . To prevent evaporation, wells in the two outer rows were always filled with water and the plate was sealed with a transparent sticker. Measurements were performed using a Tecan Spark microplate reader. Fluorescence intensity was recorded every 6 min using the bottom readout with continuous linear shaking in between. The excitation and emission wavelength ranges were controlled using filters (430 nm with  $20 \text{ nm}$  bandwidth and 460 nm with  $20 \text{ nm}$  bandwidth, respectively). Four measurements were done for every individual data point. To extract  $t_{50}$  from the ThT fluorescence traces, we fitted a simple aggregation model (as described previously)<sup>11</sup> and used the time to reach 50% of the max signal.

## NMR spectroscopy

To determine the partition coefficient of ATP, a  $10 \text{ ml}$  condensate suspension containing  $2.4 \text{ mM}$  pLys,  $2.4 \text{ mM}$  pGlu, and  $0.5 \text{ mM}$  ATP in standard buffer with  $10\%$  D<sub>2</sub>O was centrifuged for 30 min at  $500 \times g$  at

$20^\circ\text{C}$ . The phases were separated and  $12.5 \mu\text{L}$  condensate phase was obtained, which was diluted 40 times to  $500 \mu\text{L}$  using  $1 \text{ M}$  NaCl<sup>72</sup>. The supernatant was used without further dilution. Subsequently, hexamethylphosphoramido was added to the separated phases, with a final concentration of  $4 \text{ mM}$  for the condensate phase sample and  $10 \text{ mM}$  for the dilute phase sample. <sup>31</sup>P NMR spectra were recorded on a Bruker-Avance III 500 spectrometer at  $500 \text{ MHz}$ . A pulse sequence was set up with 8 transients ( $nt = 8$ ),  $P1 = 13 \text{ ms}$ , which corresponds to approximately a  $90^\circ$  pulse angle and a  $d_1$  relaxation delay of  $30 \text{ s}$ , in order to ensure full relaxation of nuclei. The data was processed with MestReNova 14. The ATP concentration was calculated by taking the mean integral of the  $\alpha$  ( $-5.5 \text{ ppm}$ ),  $\beta$  ( $-10.5 \text{ ppm}$ ), and  $\gamma$  ( $-20.7 \text{ ppm}$ ) phosphate peaks. An ATP concentration of  $101.2 \text{ mM}$  and  $0.22 \text{ mM}$  was calculated in the condensate phase and dilute phase, respectively, resulting in a partition coefficient of 462.

## Fusion of suspended droplets using optical traps

Fusion assays in optical traps were performed to determine the inverse capillary velocity of condensates, based on protocols from refs. 73, 74. Fusion events were tracked using a LUMICKS C-Trap dual-trap OT instrument. Measurements were performed in Ibidi single-channel slides ( $\mu$ -Slide I Luer,  $0.4 \text{ mm}$ , polymer bottom). Channel slides were modified with PLL-g[3.5]-PEG using the same protocol as for the glass slides, but using  $0.003 \text{ mg/ml}$  PLL-g[3.5]-PEG concentration, which is important for the further active rheology measurements performed in the same slides. The condensate samples were first mixed in an Eppendorf tube, then the suspension was transferred into the channel slide and placed at the OT instrument. Both traps were first set to intermediate power with ca.  $30 \mu\text{m}$  distance between them to scavenge nearby condensate droplets. When the trapped droplets reached the desired size ( $5\text{--}10 \mu\text{m}$  in diameter), the droplet in trap 1 was moved close to the droplet in trap 2. Subsequently, trap 1 was moved at a constant speed of  $0.1 \mu\text{m/s}$  in the direction of trap 2 until fusion of the droplets was observed. The force-time response from both traps was recorded at  $78.125 \text{ kHz}$  sampling frequency and analyzed using the following model:

$$F = a + H(t - t_0) \cdot [b(1 - e^{-(t-t_0)/\tau}) + c(t - t_0)] \quad (1)$$

Where  $a$  and  $a + b$  are the pre-fusion and post-fusion force plateau,  $t_0$  is the starting time of the fusion event,  $H(t - t_0)$  is a Heaviside step function applying the exponential term only after time  $t_0$ ,  $\tau$  is the fusion relaxation time and  $c(t - t_0)$  is a linear term compensating for the trap movement. The fusion time is used as measure proportional to  $\frac{\eta}{\eta'}$ , which we use to calculate the surface tension.

## Active rheology using an optical trap

Active rheology inside condensate droplets to measure interfacial tension and viscosity of condensates was performed by oscillating polystyrene beads, based on the protocol from ref. 75. After condensate droplets sedimented to the bottom of the channel slide and coalesced into larger droplets,  $1 \mu\text{l}$  of Fluoresbrite Yellow Green Microspheres ( $1 \mu\text{m}$  diameter) suspension was added to the slide. A single bead per coacervate was either trapped in solution and dragged into the droplet, or a bead that was already present inside droplets was used. From the oscillation data,  $G'$  and  $G''$  were calculated and fit with a single-mode Maxwell model.  $\eta_0 = F_0 \tau_0$  was calculated at zero-shear according to  $\eta_0 = F_0 \tau_0$ .

## Reporting summary

Further information on research design is available in the Nature Portfolio Reporting Summary linked to this article.

## Data availability

The source data generated in this study have been deposited in the Radboud Repository [<https://data.ru.nl>] under the <https://doi.org/10.34973/k3ba-g894>. The data are available under CC-BY-4.0 license. Unless otherwise stated, all data supporting the results of this study can be found in the article, supplementary, and source data files. Source Data are provided with this paper.

## Code availability

The code used in this study have been deposited in the Radboud Repository [<https://data.ru.nl>] under the <https://doi.org/10.34973/k3ba-g894>. The data are available under CC-BY-4.0 license.

## References

- Irwin, D. J., Lee, V. M. Y. & Trojanowski, J. Q. Parkinson's disease dementia: convergence of  $\alpha$ -synuclein, tau and amyloid- $\beta$  pathologies. *Nat. Rev. Neurosci.* **14**, 626–636 (2013).
- Brunello, C. A., Merezhko, M., Uronen, R. L. & Huttunen, H. J. Mechanisms of secretion and spreading of pathological tau protein. *Cell. Mol. Life Sci.* **77**, 1721–1744 (2020).
- Chen, G. F. et al. Amyloid beta: structure, biology and structure-based therapeutic development. *Acta Pharm. Sin.* **38**, 1205–1235 (2017).
- Linse, S. Mechanism of amyloid protein aggregation and the role of inhibitors. *Pure Appl. Chem.* **91**, 211–229 (2019).
- Meisl, G. et al. Uncovering the universality of self-replication in protein aggregation and its link to disease. *Sci. Adv.* **8**, e6831 (2022).
- Grigolato, F. & Arosio, P. The role of surfaces on amyloid formation. *Biophys. Chem.* **270**, 106533 (2021).
- Grigolato, F., Colombo, C., Ferrari, R., Rezabkova, L. & Arosio, P. Mechanistic origin of the combined effect of surfaces and mechanical agitation on amyloid formation. *ACS Nano* **11**, 11358–11367 (2017).
- Roeters, S. J. et al. Elevated concentrations cause upright alpha-synuclein conformation at lipid interfaces. *Nat. Commun.* **14**, 1–12 (2023).
- Campioni, S. et al. The presence of an air-water interface affects formation and elongation of  $\alpha$ -synuclein fibrils. *J. Am. Chem. Soc.* **136**, 2866–2875 (2014).
- Morinaga, A. et al. Critical role of interfaces and agitation on the nucleation of A $\beta$  amyloid fibrils at low concentrations of A $\beta$  monomers. *Biochim. Biophys. Acta Proteins Proteom.* **1804**, 986–995 (2010).
- Lipiński, W. P. et al. Biomolecular condensates can both accelerate and suppress aggregation of  $\alpha$ -synuclein. *Sci. Adv.* **8**, eabq6495 (2022).
- Shen, Y. et al. The liquid-to-solid transition of FUS is promoted by the condensate surface. *Proc. Natl. Acad. Sci. USA* **120**, e2301366120 (2023).
- Linsenmeier, M. et al. The interface of condensates of the hnRNP A1 low-complexity domain promotes formation of amyloid fibrils. *Nat. Chem.* **15**, 1340–1349 (2023).
- He, C., Wu, C. Y., Li, W. & Xu, K. Multidimensional super-resolution microscopy unveils nanoscale surface aggregates in the aging of FUS condensates. *J. Am. Chem. Soc.* **145**, 24240–24248 (2023).
- van Haren, M. H. I., Visser, B. S. & Spruijt, E. Probing the surface charge of condensates using microelectrophoresis. *Nat. Commun.* **15**, 1–10 (2024).
- Posey, A. E. et al. Biomolecular condensates are characterized by interphase electric potentials. *J. Am. Chem. Soc.* **146**, 28268–28281 (2024).
- Majee, A., Weber, C. A. & Jülicher, F. Charge separation at liquid interfaces. *Phys. Rev. Res.* **6**, 033138 (2024).
- Yu, W. et al. Aging-dependent evolving electrochemical potentials of biomolecular condensates regulate their physicochemical activities. *Nat. Chem.* **17**, 756–766 (2025).
- Hoffmann, C. et al. Electric potential at the interface of membraneless organelles gauged by graphene. *Nano Lett.* **23**, 10796–10801 (2023).
- Lee, C. Y. S., et al. Recruitment of mRNAs to P granules by condensation with intrinsically-disordered proteins. *Elife* **9**, e52896 (2020).
- Mollet, S. et al. Translationally repressed mRNA transiently cycles through stress granules during stress. *Mol. Biol. Cell* **19**, 4469–4479 (2008).
- Aye, H. M., Li, F. J. & He, C. Y. Dynamic composition of stress granules in *Trypanosoma brucei*. *PLoS Pathog.* **20**, e1012666 (2024).
- Buchan, J. R., Yoon, J. H. & Parker, R. Stress-specific composition, assembly and kinetics of stress granules in *Saccharomyces cerevisiae*. *J. Cell Sci.* **124**, 228–239 (2011).
- Chen, Y. et al. 14-3-3/Tau interaction and tau amyloidogenesis. *J. Mol. Neurosci.* **68**, 620–630 (2019).
- Zagrovic, B., Bartonek, L. & Polyansky, A. A. RNA-protein interactions in an unstructured context. *FEBS Lett.* **592**, 2901–2916 (2018).
- Norstrom, E. M. & Mastrianni, J. A. The charge structure of helix 1 in the prion protein regulates conversion to pathogenic PrPSc. *J. Virol.* **80**, 8521 (2006).
- Mompeán, M., Chakrabarty, A., Buratti, E. & Laurents, D. V. Electrostatic repulsion governs TDP-43 C-terminal domain aggregation. *PLoS Biol.* **14**, e1002447 (2016).
- Burré, J. The synaptic function of  $\alpha$ -synuclein. *J. Parkinsons Dis.* **5**, 699–713 (2015).
- Makasewicz, K. et al. Tipping point in  $\alpha$ -synuclein-membrane interactions from stable protein-covered vesicles to amyloid aggregation. *Cell Rep. Phys. Sci.* **5**, 102309 (2024).
- Bjellqvist, B. et al. The focusing positions of polypeptides in immobilized pH gradients can be predicted from their amino acid sequences. *Electrophoresis* **14**, 1023–1031 (1993).
- Bjellqvist, B., Basse, B., Olsen, E. & Celis, J. E. Reference points for comparisons of two-dimensional maps of proteins from different human cell types defined in a pH scale where isoelectric points correlate with polypeptide compositions. *Electrophoresis* **15**, 529–539 (1994).
- Leurs, Y. H. A. et al. Stabilization of condensate interfaces using dynamic protein insertion. *J. Am. Chem. Soc.* **147**, 18412–18418 (2025).
- Farag, M. et al. Condensates formed by prion-like low-complexity domains have small-world network structures and interfaces defined by expanded conformations. *Nat. Commun.* **13**, 1–15 (2022).
- Wang, J. et al. Sequence-dependent conformational transitions of disordered proteins during condensation. *Chem. Sci.* **15**, 20056–20063 (2024).
- Pyo, A. G. T., Zhang, Y. & Wingreen, N. S. Proximity to criticality predicts surface properties of biomolecular condensates. *Proc. Natl. Acad. Sci. USA* **120**, e2220014120 (2023).
- Galvanetto, N. et al. Extreme dynamics in a biomolecular condensate. *Nature* **619**, 876–883 (2023).
- Bauer, D. J. & Nikoubashman, A. The conformations of protein chains at the interface of biomolecular condensates. *Nat. Commun.* **15**, 1–4 (2024).
- Digman, M. A. et al. Fluctuation correlation spectroscopy with a laser-scanning microscope: exploiting the hidden time structure. *Biophys. J.* **88**, L33–L36 (2005).
- Schmidt, H. B., Barreau, A. & Rohatgi, R. Phase separation-deficient TDP43 remains functional in splicing. *Nat. Commun.* **10**, 1–14 (2019).
- Traut, T. W. Physiological concentrations of purines and pyrimidines. *Mol. Cell Biochem.* **140**, 1–22 (1994).
- Hautke, A. & Ebbinghaus, S. The emerging role of ATP as a cosolute for biomolecular processes. *Biol. Chem.* **404**, 897–908 (2023).

42. Pathak, D. et al. The role of mitochondrially derived ATP in synaptic vesicle recycling. *J. Biol. Chem.* **290**, 22325–22336 (2015).
43. Rangaraju, V., Calloway, N. & Ryan, T. A. Activity-driven local ATP synthesis is required for synaptic function. *Cell* **156**, 825–835 (2014).
44. Greiner, J. V. & Glonek, T. Intracellular ATP concentration and implication for cellular evolution. *Biology (Basel)* **10**, 1166 (2021).
45. Rice, A. M. & Rosen, M. K. Cell biology: ATP controls the crowd. *Science* **356**, 701–702 (2017).
46. Luk, K. C., Mills, I. P., Trojanowski, J. Q. & Lee, V. M. Y. Interactions between Hsp70 and the hydrophobic core of  $\alpha$ -synuclein inhibit fibril assembly. *Biochemistry* **47**, 12614–12625 (2008).
47. Dedmon, M. M., Christodoulou, J., Wilson, M. R. & Dobson, C. M. Heat shock protein 70 inhibits  $\alpha$ -synuclein fibril formation via preferential binding to prefibrillar species. *J. Biol. Chem.* **280**, 14733–14740 (2005).
48. Duennwald, M. L., Echeverria, A. L. & Shorter, J. Small heat shock proteins potentiate amyloid dissolution by protein disaggregases from yeast and humans. *PLoS Biol.* **10**, e1001346 (2012).
49. Gao, X. et al. Human Hsp70 disaggregase reverses Parkinson's-linked  $\alpha$ -synuclein amyloid fibrils. *Mol. Cell* **59**, 781–793 (2015).
50. Tao, J. et al. Hsp70 chaperone blocks  $\alpha$ -synuclein oligomer formation via a novel engagement mechanism. *J. Biol. Chem.* **296**, 100613 (2021).
51. Frottin, F. et al. The nucleolus functions as a phase-separated protein quality control compartment. *Science* **365**, 342–347 (2019).
52. Klucken, J., Shin, Y., Masliah, E., Hyman, B. T. & McLean, P. J. Hsp70 reduces  $\alpha$ -synuclein aggregation and toxicity. *J. Biol. Chem.* **279**, 25497–25502 (2004).
53. Pemberton, S. et al. Hsc70 protein interaction with soluble and fibrillar  $\alpha$ -synuclein. *J. Biol. Chem.* **286**, 34690–34699 (2011).
54. Kelley, F. M., Favetta, B., Regy, R. M., Mittal, J. & Schuster, B. S. Amphiphilic proteins coassemble into multiphasic condensates and act as biomolecular surfactants. *Proc. Natl. Acad. Sci. USA* **118**, e2109967118 (2021).
55. Fakhree, M. A. A. et al. The localization of alpha-synuclein in the endocytic pathway. *Neuroscience* **457**, 186–195 (2021).
56. Fakhree, M. A. A., Nolten, I. S., Blum, C. & Claessens, M. M. A. E. Different conformational subensembles of the intrinsically disordered protein  $\alpha$ -synuclein in cells. *J. Phys. Chem. Lett.* **9**, 1249–1253 (2018).
57. Kurochka, A. S., Yushchenko, D. A., Bouř, P. & Shvadchak, V. V. Influence of lipid membranes on  $\alpha$ -synuclein aggregation. *ACS Chem. Neurosci.* **12**, 825–830 (2021).
58. Makasewicz, K. et al. Cooperativity of  $\alpha$ -synuclein binding to lipid membranes. *ACS Chem. Neurosci.* **12**, 2099–2109 (2021).
59. Galvagnion, C. et al. Lipid vesicles trigger  $\alpha$ -synuclein aggregation by stimulating primary nucleation. *Nat. Chem. Biol.* **11**, 229–234 (2015).
60. Zhou, J. et al. Effects of sedimentation, microgravity, hydrodynamic mixing and air–water interface on  $\alpha$ -synuclein amyloid formation. *Chem. Sci.* **11**, 3687–3693 (2020).
61. Vaneyck, J., Segers-Nolten, I., Broersen, K. & Claessens, M. M. A. E. Cross-seeding of alpha-synuclein aggregation by amyloid fibrils of food proteins. *J. Biol. Chem.* **296**, 100358 (2021).
62. Havemeister, F., Ghaeidamini, M. & Esbjörner, E. K. Monovalent cations have different effects on the assembly kinetics and morphology of  $\alpha$ -synuclein amyloid fibrils. *Biochem. Biophys. Res. Commun.* **679**, 31–36 (2023).
63. Sidhu, A., Segers-Nolten, I. & Subramaniam, V. Solution conditions define morphological homogeneity of  $\alpha$ -synuclein fibrils. *Biochim. Biophys. Acta (BBA) - Proteins Proteom.* **1844**, 2127–2134 (2014).
64. André, A. A. M. *Artificial Membraneless Organelles in Crowded Environments* (Radboud, 2024).
65. Nott, T. J., Craggs, T. D. & Baldwin, A. J. Membraneless organelles can melt nucleic acid duplexes and act as biomolecular filters. *Nat. Chem.* **8**, 569–575 (2016).
66. Javed, S. & Spruijt, E. Spontaneous wrapping of coacervates by lipid bilayers upon heat shock creates resilient and intact membranized coacervates. <https://doi.org/10.26434/CHEMRXIV-2024-F4GLS> (2024).
67. Pir Cakmak, F., Grigas, A. T. & Keating, C. D. Lipid vesicle-coated complex coacervates. *Langmuir* **35**, 7830–7840 (2019).
68. Petrášek, Z. & Schwille, P. Precise measurement of diffusion coefficients using scanning fluorescence correlation spectroscopy. *Biophys. J.* **94**, 1437–1448 (2008).
69. Schrimpf, W., Barth, A., Hendrix, J. & Lamb, D. C. PAM: a framework for integrated analysis of imaging, single-molecule, and ensemble fluorescence data. *Biophys. J.* **114**, 1518–1528 (2018).
70. Levine, H. Thioflavine T interaction with synthetic Alzheimer's disease beta-amyloid peptides: detection of amyloid aggregation in solution. *Protein Sci.* **2**, 404 (1993).
71. Naiki, H., Higuchi, K., Hosokawa, M. & Takeda, T. Fluorometric determination of amyloid fibrils in vitro using the fluorescent dye, thioflavine T. *Anal. Biochem.* **177**, 244–249 (1989).
72. Smokers, I. B. A. & Spruijt, E. Quantification of Biomolecular Condensate Volume Reveals Network Swelling and Dissolution Regimes during Phase Transition. *Biomacromolecules* **26**, 363–373 (2025).
73. Ghosh, A. & Zhou, H. X. Determinants for fusion speed of biomolecular droplets. *Angew. Chem. - Int. Ed.* **59**, 20837–20840 (2020).
74. Alshareedah, I., Thurston, G. M. & Banerjee, P. R. Quantifying viscosity and surface tension of multicomponent protein-nucleic acid condensates. *Biophys. J.* **120**, 1161–1169 (2021).
75. Ghosh, A., Kota, D. & Zhou, H. X. Shear relaxation governs fusion dynamics of biomolecular condensates. *Nat. Commun.* **12**, 1–10 (2021).
76. Goodsell, D. S., Autin, L. & Olson, A. J. Illustrate: software for biomolecular illustration. *Structure* **27**, 1716–1720.e1 (2019).
77. Li, J., Uversky, V. N. & Fink, A. L. Effect of familial Parkinson's disease point mutations A30P and A53T on the structural properties, aggregation, and fibrillation of human  $\alpha$ -synuclein. *Biochemistry* **40**, 11604–11613 (2001).

## Acknowledgements

This work was supported financially by a Vidi grant from the Netherlands Organization for Scientific Research (NWO) to E.S., the European Research Council (ERC) under grant agreement number 851963 to E.S.M.V.A.Q. acknowledges financial support from the São Paulo Research Foundation (FAPESP) under project number 2023/12135-0. M.M.A.E.C. and E.S. are principal investigators of the Gravitation Consortium "FLOW" (024.006.036), funded by the Dutch Ministry of Education, Culture, and Science (OCW). The authors would like to thank Dr. Alain A.M. André for expression and purification of EGFP-NPM1 and GFP-G3BP1, Prof. Sushma N. Grellscheid for providing U2OS cells expressing GFP-G3BP1, Dr. N. Amy Yewdall for purification of DDX4-YFP, Jonathan Hoekstra for help in purifying TDP-43-TEV-mCherry, and Dr. Tim Nott for sharing the Ddx4N1YFP pETM30 vector.

## Author contributions

B.S.V., W.P.L., M.H.I.vH., and E.S. conceived the project. B.S.V., W.P.L., designed and performed the confocal microscopy experiments. M.H.I.vH. performed and analyzed the  $\zeta$ -potential experiments. W.P.L. wrote the code for surface adsorption analysis. K.A.vL., M.M.A.E.C., M.V.A.Q., J.E., and C.H.I.R., provided resources. B.S.V., W.P.L., M.H.I.vH., and E.S. analyzed the data and wrote the manuscript. B.S.V., W.P.L., M.H.I.vH., MM.A.E.C., M.V.A.Q., C.H.I.R., J.E., and E.S., reviewed and edited the manuscript. E.S. supervised the project.

**Competing interests**

The authors declare no competing interests.

**Additional information**

**Supplementary information** The online version contains supplementary material available at  
<https://doi.org/10.1038/s41467-025-65030-5>.

**Correspondence** and requests for materials should be addressed to Evan Spruijt.

**Peer review information** *Nature Communications* thanks the anonymous reviewers for their contribution to the peer review of this work. A peer review file is available.

**Reprints and permissions information** is available at  
<http://www.nature.com/reprints>

**Open Access** This article is licensed under a Creative Commons Attribution-NonCommercial-NoDerivatives 4.0 International License, which permits any non-commercial use, sharing, distribution and reproduction in any medium or format, as long as you give appropriate credit to the original author(s) and the source, provide a link to the Creative Commons licence, and indicate if you modified the licensed material. You do not have permission under this licence to share adapted material derived from this article or parts of it. The images or other third party material in this article are included in the article's Creative Commons licence, unless indicated otherwise in a credit line to the material. If material is not included in the article's Creative Commons licence and your intended use is not permitted by statutory regulation or exceeds the permitted use, you will need to obtain permission directly from the copyright holder. To view a copy of this licence, visit <http://creativecommons.org/licenses/by-nc-nd/4.0/>.

© The Author(s) 2025

**Publisher's note** Springer Nature remains neutral with regard to jurisdictional claims in published maps and institutional affiliations.